www.MaterialsViews.com

ADVANCED
MATERIALS
INTERFACES
www.advmatinterfaces.de

FULL PAPER

Quasi 2D Ultrahigh Carrier Density in a Complex Oxide Broken-Gap Heterojunction

Peng Xu, Timothy C. Droubay, Jong Seok Jeong, K. Andre Mkhoyan, Peter V. Sushko, Scott A. Chambers, and Bharat Jalan*

Two-dimensional (2D) ultra-high carrier densities are of considerable current research interest for novel plasmonic and high charge-gain devices. However, the highest 2D electron density obtained is thus far limited to 3×10^{14} cm^{-2} (½ electron/unit cell/interface) at $GdTiO_3$/$SrTiO_3$ interfaces, and is typically an order of magnitude lower at $LaAlO_3$/$SrTiO_3$ interfaces. We show from experiment and modeling that carrier densities much higher than expected based on resolution of the polar discontinuity at perovskite oxide heterojunctions can be achieved via band engineering. The $SrTiO_3$ (8 u.c.)/ $NdTiO_3$ (t u.c.) /$SrTiO_3$ (8 u.c.) /LSAT(001) heterostructure shows the expected electronic reconstruction behavior starting at $t = 2$ u.c., but then exhibits a higher carrier density regime at $t \geq 6$ u.c. due to additional charge transfer from band alignment.

1. Introduction

Heterostructure engineering leading to 2D carrier densities enables the design of new classes of materials with desirable functionalities and useful applications.[1–3] Complex oxide heterostructures can show strong correlation effects, novel magnetism, high breakdown voltage, and high 2D electron density (of the order of 10^{14} cm^{-2}), unattainable in traditional semiconductor heterostructures.[4–13] High 2D electron densities are of particular interest for studying low-dimensional physics in narrow *d*-band materials, in addition to fabricating novel plasmonic field-effect transistors (FETs).[14–16] Specifically, plasmonic FETs require a high 2D carrier density, but high mobility is not needed.[14] The plasma wave velocity, which forms the basis for plasmonic devices, is directly proportional to the 2D electron density (2DEG). This requirement is in contrast to traditional FETs in which a high saturation velocity for electrons, which is inversely proportional to the carrier density, is required.[15] Structures realizing ultrahigh-density 2DEG may thus be transformative and could serve as building blocks for novel oxide electronics such as plasmonic FETs. There are,

however, only a few oxides accommodating high electron density confined to low dimensions.[12,17–21] Filling this materials gap would provide qualitatively new opportunities in the field of nanoscale oxide electronic devices including novel plasmonic and high charge-gain devices.

$NdTiO_3$ (NTO) and $SrTiO_3$ (STO) are classified as a Mott and a band insulator, respectively. Moreover, the interface formed between polar NTO and nonpolar STO is metallic.[22] NTO/STO is thus expected to exhibit a 2DEG equivalent to 0.5 electron (e$^-$) per lateral unit cell per interface. Here, we report the discovery of a quasi-2D ultrahigh-density electron gas exceeding 3×10^{15} cm^{-2}, which is tunable by means of the NTO film thickness in molecular beam epitaxy (MBE)-grown heterostructures. This novel quasi-2DEG results from a broken-gap band alignment[23,24] at the NTO/STO interface, which we have experimentally detected and theoretically verified. We note that such band alignments, which also form the basis for a low-power tunnel FETs, are rare.[1] They have been positively identified in traditional III–V semiconductor heterostructures[24] and 2D crystals,[25] and have only indirectly been associated with oxide heterostructures.[26–32]

2. Results and Discussion

We begin by discussing the structural properties of the NTO/STO interface, which are critical to establishing a credible case for the electronic structure. **Figure 1**a shows a representative high-angle annular dark-field scanning transmission electron microscopy (HAADF-STEM) image of a 35 nm thick cross section of an NTO/STO (001) superlattice along the [100] zone axis of the substrate. The image reveals continuous, coherent, highly planar layers, which extend over long lateral distances with no gross structural defects or secondary phases. Figure 1b shows the accompanying grazing incidence X-ray reflectivity (GIXR) scan, which exhibits Kiessig fringes and sharp superlattice Bragg peaks, indicating high structural quality. The well-defined Kiessig fringes at low q_z between the critical angle and the first superlattice Bragg peak further attest to the highly uniform film thickness and small surface roughness (½ unit cell (u.c.)). Atomic force microscopy (AFM) images show atomically smooth surfaces (Figure 1c).

Figure 2 shows the temperature dependence of the sheet resistance (R_s) for NTO/STO/LSAT and STO/NTO/STO/LSAT heterostructures as a function of NTO thickness, with the STO

P. Xu, Prof. J. S. Jeong, Prof. K. A. Mkhoyan, Prof. B. Jalan
Department of Chemical Engineering
and Materials Science
University of Minnesota
Minneapolis, MN 55455, USA
E-mail: bjalan@umn.edu
Dr. T. C. Droubay, Dr. P. V. Sushko, Dr. S. A. Chambers
Physical Sciences Division
Physical & Computational Sciences Directorate
Pacific Northwest National Laboratory
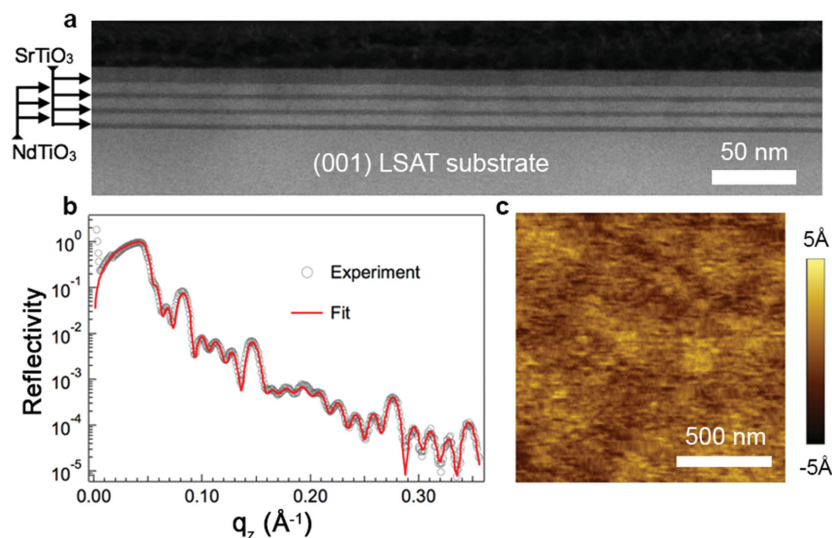Richland, WA 99352, USA

Figure 1. a) High angle annular dark field (HAADF)-scanning transmission electron microscopy (STEM) image of a NTO/STO superlattice grown on LSAT (001) substrate, b) grazing incident X-ray reflectivity of this structure along with a fit yielding $t_{NTO} = 6$ nm, and $t_{STO} = 3$ nm, c) AFM image of the superlattice with root mean square roughness, 0.15 nm.

thickness held constant at 8 u.c. For the uncapped NTO/STO samples (Figure 2a), there is no measurable conductivity for $t < 4$ u.c. However, an insulator-to-metal transition occurs at $t \geq 4$ u.c. with two distinct metallic regimes: i) high R_s (8 u.c. $\leq t \leq 12$ u.c.) and ii) low R_s ($t > 12$ u.c.) (Figure 2b). Hall measurements show n-type behavior with a 2D electron density (n_{2D}) of ≈ 0.5 e$^-$ per u.c. per interface ($\approx 3 \times 10^{14}$ cm^{-2}) and a critical thickness of 10 u.c., followed by an increase leading to saturation at higher t (Figure 2c). The first metallic regime results from electronic reconstruction. The second results from charge transfer associated with band alignment, as explained in conjunction with **Figure 3**.

In contrast, metallic behavior is observed for $t \geq 2$ u.c. in the STO-capped heterostructures (Figure 2d,e). The much higher conductivity threshold in the uncapped system is most likely due to NTO surface chemical modification resulting from air exposure, and indicates that surface reactivity can have a strong influence on interfacial conductivity.[33] Indeed, X-ray photoelectron spectroscopy (XPS) measurements reveal the presence of both OH and organic contamination on the surfaces of all specimens and, apparently, that reactions with atmospheric humidity and/or organics chemically alter the NTO to the point that its electronic properties no longer facilitate conductive interface formation with STO. Figure 2f shows room-temperature n_{2D} versus t with a nearly constant value of ≈ 1 e$^-$ per u.c. (equivalent to 0.5 e$^-$ per u.c. per interface) up to ≈ 6 u.c., followed by a monotonic increase and no indication of saturation with t. As with the uncapped samples, this marks a transition from one metallic regime resulting from electronic reconstruction to another resulting from charge transfer driven by band alignment. This transition at 6 u.c., although not stark in Figure 2f, is more apparent in the R_s (t) data (see Figure S1 in the Supporting Information). From these data, the critical thickness for this transition is clearly 6 u.c. It is noteworthy that unlike the LaAlO$_3$/STO system, the capped

heterostructures become conductive starting at only 2 u.c. of NTO, with a carrier density of ≈ 0.5 e$^-$ per u.c. per interface. As pointed out by Janotti et al.,[34] this is precisely what is expected for a polar perovskite forming an interface with a nonpolar perovskite. Each NdO layer in contact with STO dopes 0.5 e$^-$ per u.c. into the adjacent STO, and no minimum thickness for conduction is expected.[35] As we have found, both capped and uncapped heterostructures show a n_{2D} value of ≈ 0.5 e$^-$ per u.c. per interface up to a critical thickness, above which the carrier concentration increases. This observation corroborates the existence of the two distinct metallic regimes in Figure 2b,e and will further be illustrated in Figure 5. As described below, neither cation intermixing nor oxygen vacancy nonstoichiometry can explain the increase in n_{2D} above the critical thickness. Additionally, the fact that the n_{2D} values decrease and the R_s values increase when the stoichiometry is suboptimal[22] is also consistent with cation nonstoichiometry not being the driver of conduction in this regime. Rather, our XPS measurements reveal that the most likely physical cause for the higher n_{2D} values above the critical thickness is charge transfer due to a broken-gap band alignment, as discussed below.

We performed band offset measurements using high-resolution XPS[36–39] for an NTO/STO sample set. The binding energy difference between the shallow Sr 3d and Nd 4d core levels was utilized to obtain the valence band offset (VBO). Doing so requires measurement of the energy difference between these two core levels and the associated valence band maxima (VBM) for a thick film of NTO (001) and a bulk STO (001) single crystal, respectively. We found these energy differences to be 122.34 (14) eV for Nd 4d (Figure 3b) and 130.54 (3) eV[37] for Sr 3d. The error is much larger for Nd 4d than for Sr 3d because of the extreme breadth of the former and the weak photoemission intensity at the leading edge of the lower Hubbard band in NTO, as seen in Figure 3a,b. With these values, we determined the VBO to be consistently 3.2 (2) eV for NTO thicknesses of 2, 4, 6, and 8 u.c. on STO, as well as for a 3 u.c. STO/18 u.c. NTO inverted interface on LSAT. Assuming the band gaps of STO and NTO are 3.2 and 0.8 eV,[40] respectively, Figure 3c illustrates that the top of the lower Hubbard band (LHB) in NTO is equilibrated with the conduction band minimum (CBM) of STO, as expected for a type-II broken-gap band alignment and the associated charge transfer. We note that the observed broken-gap alignment is unique and fundamentally different from classical semiconductor heterostructures in that it is between the CBM of STO and the LHB of NTO arising from Mott physics.

Given that the LHB of NTO and the CB of STO are derived primarily from Ti 3d orbitals,[41] a change in Ti valence is expected to accompany charge transfer. Specifically, if electrons from NTO spill over into the STO, the Ti oxidation state will exceed 3+ in the NTO and be less than 4+ in the STO. These changes in Ti valence are indeed observed in our STEM electron
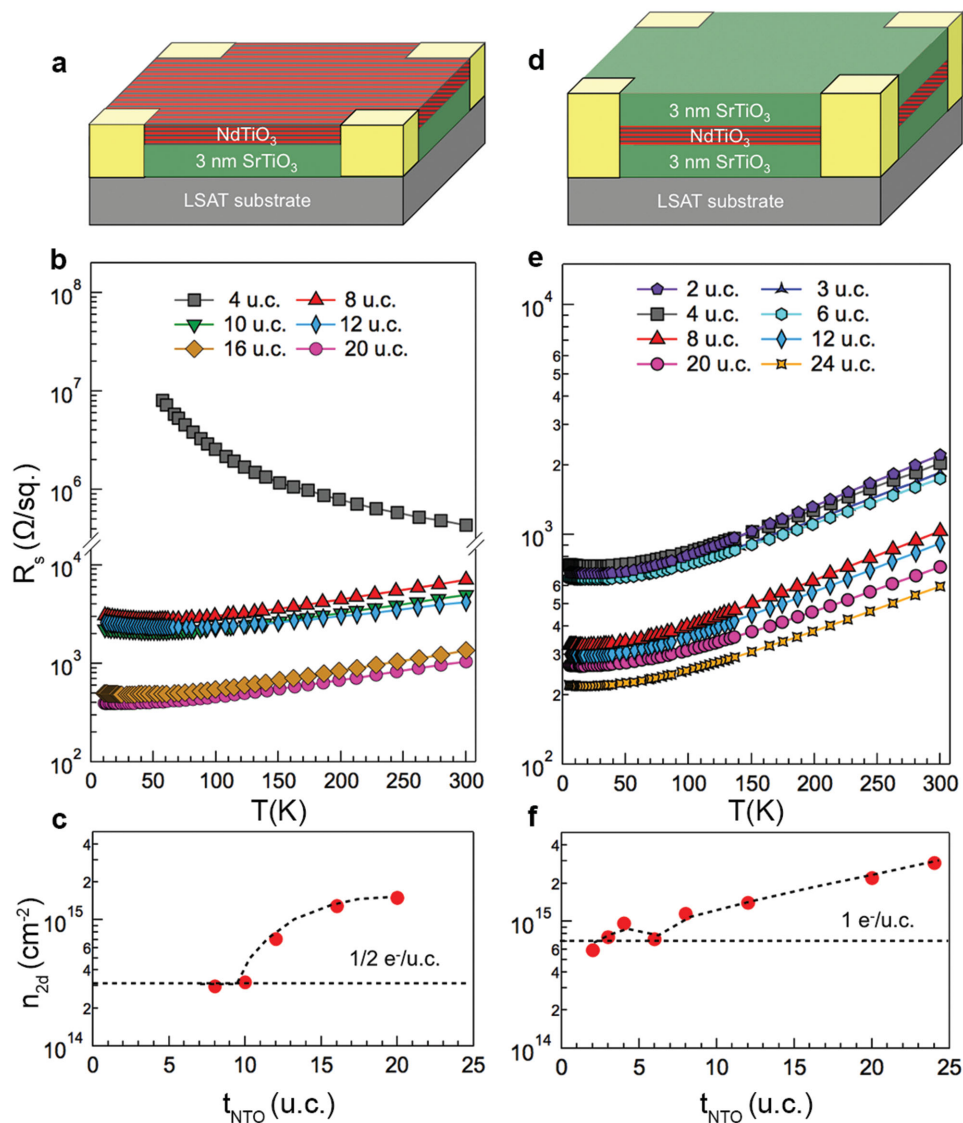
Materials
Views
www.MaterialsViews.com

ADVANCED
MATERIALS
INTERFACES
www.advmatinterfaces.de

FULL PAPER

Figure 2. Device schematics for a) NTO/STO/LSAT and d) STO/NTO/STO/LSAT heterostructures. Temperature dependence of the sheet resistance (R_s) for b) NTO/STO/LSAT and e) STO/NTO/STO/LSAT. 2D electron density (n_{2D}) as a function of NTO thickness for c) NTO/STO/LSAT and f) STO/NTO/STO/LSAT. The dashed lines are a guide to the eye. The radius of the circles denoting the data points in panels (c) and (f) equals the error bar in carrier concentrations.

energy loss spectroscopy (STEM-EELS) data, and are far more spatially extensive than what is expected based on either unintentional doping due to cation mixing or oxygen vacancy (V_O) creation (see Figures S3 and S4 in the Supporting Information). HAADF-STEM images and EELS spectra for a $\{[NTO]_{16}/[STO]_8\}_3$ superlattice are shown in **Figure 4**. The asymmetry in the Ti^{3+} profile (Figure 4b) across the STO/NTO/STO interfaces is due to an asymmetry in the structure; the bottom STO layer in Figure 4c has one interface to NTO, whereas the top STO layer is sandwiched by two NTO blocks (see Figure 4a). We observe alternating atomically sharper and more diffuse interfaces for NTO on STO, and STO on NTO, respectively, similar to what was observed in the $LaMnO_3/SrMnO_3$ superlattice.[42] While the origin of this behavior is not yet understood, both the HAADF intensity profiles (Figure 4a) and the EELS/

energy dispersive X-ray spectroscopy profiles (Figures S3 and S4, Supporting Information) show that cation mixed region is limited to 1–2 u.c. at NTO/STO, and 3–4 u.c. at STO/NTO, far smaller than the spatial extent to which Ti^{3+} (Ti^{4+}) is found in the STO (NTO). The Ti^{3+} fraction was determined by analyzing the Ti $L_{2,3}$ EELS spectra shown in Figure 4d. Position 1, which is 11 u.c. away from the interface on one STO side, exhibits a spectrum characteristic of Ti^{4+}. We superimpose on this spectrum a reference spectrum for Ti^{3+}.[43] Note that as the interface is approached, and at all points within the NTO layer, the Ti $L_{2,3}$ EELS spectra reveal a mix of Ti^{4+} and Ti^{3+}. Additionally, within the NTO film, the intensity of the sharp onset peak in the O K-edge spectra at ≈ 533 eV decreases dramatically and the broad peak at ≈ 539 eV shifts to lower energy loss, revealing changes in the low-lying unoccupied states which are largely
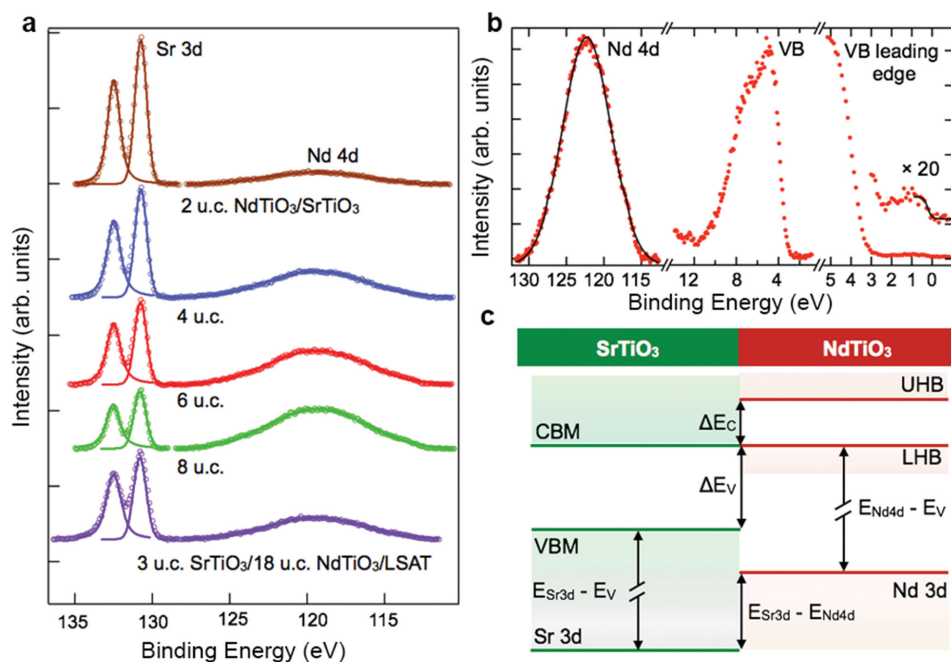
Figure 3. a) X-ray excited Sr 3d and Nd 4d core-level spectra for NTO/STO (001) with several NTO thicknesses and for the inverted interface STO (3 u.c.)/NTO (18 u.c.)/LSAT (001) heterostructure. b) The Nd 4d core peak and weak photoemission intensity on the leading edge of the lower Hubbard band in 18 u.c. NTO/LSAT (001). c) Energy-level diagram showing the measured band offsets between STO and NTO.

Ti $3d$ derived. These fine structure changes are graded across the film and are consistent with charge transfer from NTO to STO, which occurs over considerable distances, similar to what has been observed in the case of $LaTiO_3$/STO.[26] The mechanism for the large spatial extent of Ti^{3+} in STO is very likely due to no confining potential in the STO and as a result the electrons delocalize across the STO films. Our measurements

of the Sr $3d$ line shape (Figure 3a) do not reveal the broadening, which would signal the presence of strong band bending and a confining potential at the interface, and our EELS data clearly show that the Ti^{3+} (and, thus, the itinerant electrons) are not confined directly at the interface. As a result, a significant fraction of Ti^{4+} ($\approx 25\%$) is present, even in the center of the NTO film, and this cannot be accounted for based on either
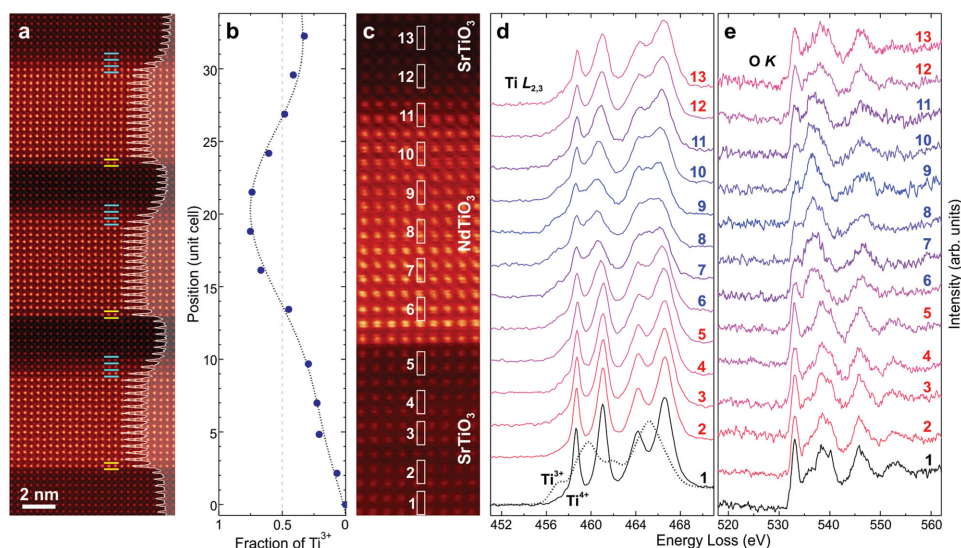

Figure 4. a) HAADF-STEM image of a $\{[NTO]_{16}/[STO]_8\}_3$ superlattice structure along with the integrated intensity profile highlighting sharper (yellow ticks) and broader (blue ticks) interfaces, b) Ti^{3+} fraction across STO/NTO/STO as shown in panel (c). The STO at the bottom is the substrate; c) STEM image of the bottom part of superlattice showing STO substrate, the first NTO film, and the first STO film, and d) Ti $L_{2,3}$ and e) O K core-loss EELS spectra measured at the positions indicated in panel (c). The Ti^{3+} fraction was obtained using linear least squares fitting to Ti^{3+} and Ti^{4+} reference spectra shown in panel (d).

cation interdiffusion or V_O creation (see Figures S3 and S4 in the Supporting Information and the related discussion).

These results raise additional questions. First, does formation of a hole gas occur in NTO due to electron transfer to STO, leading to an insulator-to-metal transition in NTO? Second, what causes the critical thickness for charge transfer over and above that expected from resolution of the polar discontinuity? NTO/STO is expected to exhibit the theoretically predicted value of 0.5 e$^-$ per u.c. per interface if no compensating defects are present. The n_{2D} value shows no obvious change as the thickness of the STO buffer layer is modified (see Figure S2c in the Supporting Information). In combination with the broken-gap band alignment measured from the XPS, this result suggests that majority carriers reside on the STO side. The room-temperature electron mobility, which remains close to that of bulk STO, further corroborates conduction within the STO (see Figure S2c in the Supporting Information). To address the question of whether or not a hole-gas conduction channel exists in the NTO, we conducted low-temperature Hall measurements on a representative pair of samples—one above and one below the NTO critical thickness (see Figure S5 in the Supporting Information). Nonlinear behavior is expected in the Hall resistance (R_{Hall} (B)), where B is the magnetic field, if more than one carrier type is responsible for conduction. However, multichannel conduction may yield linear R_{Hall} (B) behavior if the mobility and the carrier concentration of one of the carrier types are dramatically different than those of the other (see the discussion in Figure S6 in the Supporting Information). We found that both samples show a negative linear slope in R_{Hall} (B) for −9 T ≤ B ≤ +9 T. We attribute the absence of nonlinearity in R_{Hall} (B) to the different density and mobility of holes in NTO vis-a-vis those for electrons in the STO. Evidence that holes are present in the NTO is understood based on the existence of Ti^{4+} there (see Figure 4b). Given that the transition from Mott insulator to metal is sensitive to band filling of Ti 3d orbitals,[40] it is concluded that an insulator-to-metal transition has taken place in NTO due to the electron transfer to STO and corresponding hole doping of the NTO. However, the question of whether this transition accompanies the small hole-polaron

gas formation[44–46] versus a band-filling related transition is still open and requires further investigation.

We show in **Figure 5**a, the reciprocal of the total sheet resistance (1/R_S) for STO/NTO/STO/LSAT as a function of t and temperature. The reciprocal of the sheet resistance shows no change up to the critical thickness followed by a linear increase. We can describe this linear behavior using a simple model based on conduction through parallel interface layers, one from electronic reconstruction to resolve the polar discontinuity (sheet resistance = R_{PD}), and one from broken-gap-driven charge transfer (sheet resistance = R_{CT}). A linear relationship between 1/R_S and t is then expected, as is indeed observed in Figure 5a. The inverse of the total sheet resistance can be modeled as

$$\frac{1}{R_s} = \frac{2}{R_{PD}} + \frac{t_{NTO}}{R_{CT}} \qquad (1)$$

Using Equation (1), R_{PD} and R_{CT} can be determined as a function of temperature (Figure 5b). The R_{PD} values agree well with R_S values for systems having only a polar discontinuity contribution, such as GdTiO$_3$/STO.[21] R_{CT} shows metallic behavior but with an overall higher sheet resistance, consistent with an insulator-to-metal transition having taken place in NTO and contributing a larger resistance to R_{CT}.

To address the origin of the critical thickness, we seek insight into the atomic-scale mechanism(s) of charge transfer from *ab initio* simulations based on density functional theory (DFT). For the purpose of analysis of the densities of states and charge density distribution, we define the lateral unit cells in terms of [A$_1$O]$_{0.5}$ [TiO$_2$] [A$_2$O]$_{0.5}$ structural units, where A$_1$ and A$_2$ are either Sr or Nd atoms depending on the position of the layer in the heterostructure. According to this definition, the [SrO]$_{0.5}$ [TiO$_2$] [SrO]$_{0.5}$ cell in the interior of the STO and the [NdO]$_{0.5}$ [TiO$_2$] [NdO]$_{0.5}$ cell in the interior of the NTO are neutral, even if the charges of the SrO, NdO, and TiO$_2$ planes deviate from their formal values. Similarly, the interface [SrO]$_{0.5}$ [TiO$_2$] [NdO]$_{0.5}$ cell is neutral if the charge associated with the TiO$_2$ plane is equal to half the sum of the charges of SrO and NdO planes. For example, in the case of the formal charges, [SrO]^0 and [NdO]$^+$, the [SrO]$_{0.5}$ [TiO$_2$] [NdO]$_{0.5}$ cell is neutral if
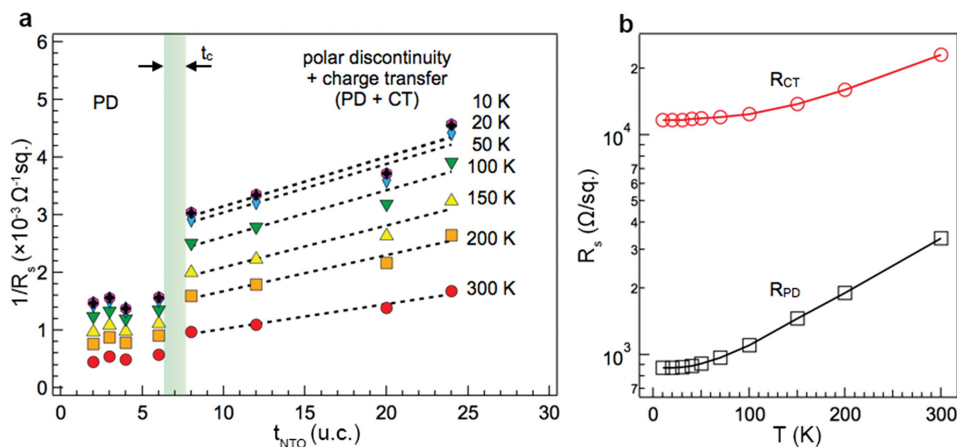

Figure 5. a) The reciprocal of the total sheet resistance (1/R_S) for STO/NTO/STO/LSAT as a function of the NTO thickness and temperature. The dashed lines are linear fits to the data. b) Sheet resistances due to resolution of the polar discontinuity (R_{PD}) and charge transfer (R_{CT}) at the interface extracted from Equation (1).
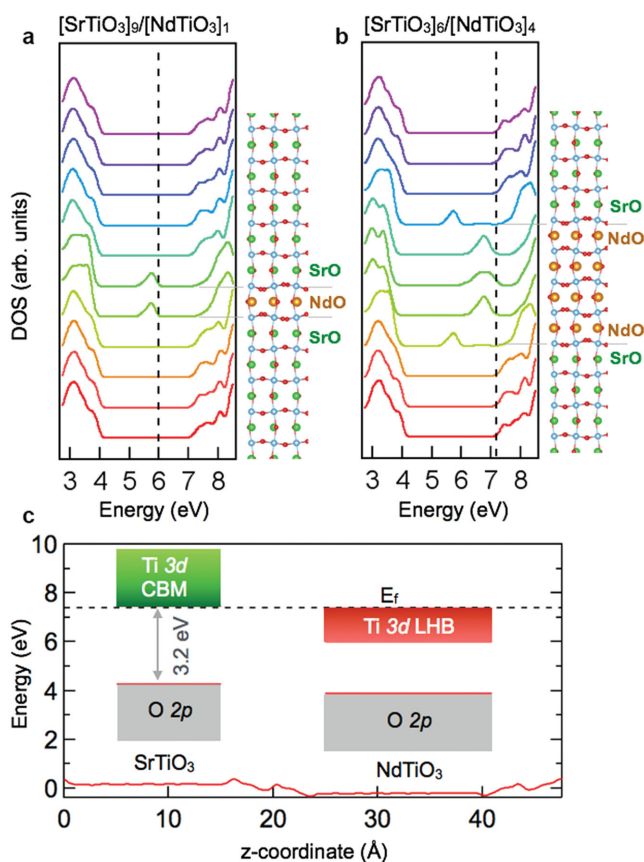
**ADVANCED
MATERIALS
INTERFACES**
www.advmatinterfaces.de

*Materials
Views*
www.MaterialsViews.com

FULL PAPER

$[NTO]_m$ (m = 4,6,8) heterostructures and the planar averaged electrostatic potential in $[STO]_6/[NTO]_6$ are shown in Figures S7 and S8 in the Supporting Information, respectively.

For all NTO thicknesses, the TiO_2 planes located between the SrO and NdO planes carry the amount of charge needed to resolve the polar discontinuity at the NTO/STO interface (formally 0.5 e⁻ per u.c. per interface), as expected for an n-type III–III/II–IV polar/nonpolar interface. Once the NTO LHB becomes degenerate with the STO CBM, additional electron charge is transferred from NTO to STO. Given the uncertainty in the measured value of the STO/NTO band offset, we investigated the dependence of the electronic structure of $[STO]_n/[NTO]_m$ and the charge transfer across the NTO/STO interface on the choice of Hubbard U correction for the Ti 3d states in STO (U_{STO}), NTO (U_{NTO}), and at the interface. The details of this analysis are summarized in the Supporting Information (see also Figures S8–S12 in the Supporting Information). In all cases the NTO is positively charged whereas the STO is negatively charged, confirming that the STO is electron-doped and the NTO is hole-doped. The amount of transferred charge depends on the thicknesses of the NTO with a maximum determined by the thickness of the STO layers; the former determines the number of electrons available for transfer, while the latter determines the width of the potential well that traps these electrons. Notably, for all values of U and for each $[STO]_n/[NTO]_m$ configuration investigated here, the positive charge appearing in NTO as a result of such charge transfer is mainly confined to the edges of the NTO layer. Yet, the charge tends to delocalize as the thickness of the NTO layer increases.

3. Conclusion

In summary, we present the first demonstration of a unique broken-gap complex oxide heterojunction showing both an ultrahigh carrier density 2DEG and nanoscale effects at the interface between STO and NTO. Recent experimental results[48] and calculations[49] for GdTiO₃/STO/GdTiO₃ heterostructures have found that a new state of matter based on a charge-ordered Mott state can be realized in the band insulator STO, suggesting a decisive role for the carrier. Therefore, the inverted heterojunction NTO/STO/NTO may provide an ideal model system to study the physics of charge-ordered states in titanates via a highly-confined STO quantum well with carrier densities much in excess of what have been previously reported. We propose that electron and hole doping via internal charge transfer may provide an exceptional route to revisit the phase diagrams of transition metal oxides in the clean limit and to fill the materials gaps by synthesizing oxides with high concentrations of carrier electrons and/or holes. Ultralow sheet resistances in thin-film heterostructures via internal charge transfer could also be useful for highly conductive electrodes for functional oxide device structures.

4. Experimental Section

NTO/STO and STO/NTO/STO structures were grown on (001) LSAT substrates (Crystech GmbH, Germany) using hybrid MBE (traditionally known as metal-organic or organometallic MBE). The STO thickness

Figure 6. Density of states for a) $[STO]_9/[NTO]_1$, and b) $[STO]_6/[NTO]_4$ heterostructures projected on the orbitals of atoms in each $[A_1O]_{0.5}[BO_2]$ $[A_2O]_{0.5}$ lateral unit cell. Vertical dashed lines indicate the Fermi energy (E_F) in each case. The calculated DOS were broadened with Gaussian functions of full width at half maximum equal to 0.2 eV. Nd, Sr, Ti, and O atoms (in the order of decreasing size) are shown with gold, green, blue, and red colors. The interface TiO_2 planes are highlighted with the gray lines. The neighboring NdO and SrO planes are explicitly labeled. c) Average electrostatic potential (red line) and E_F (dashed line) calculated for the $[STO]_6/[NTO]_6$ heterostructure strained to conform to the LSAT lattice. The positions of the O 2p and Ti 3d band edges with respect to the average electrostatic potential were calculated separately for the bulk STO and NTO, which were in turn strained to conform to the LSAT lattice.

the charge of the TiO_2 plane is −0.5, as expected from the polar discontinuity argument.

Figure 6a,b shows the density of states (DOS) calculated for $[STO]_9/[NTO]_1$ and $[STO]_6/[NTO]_4$, respectively, and projected on consecutive $[A_1O]_{0.5}[TiO_2][A_2O]_{0.5}$ lateral cells. In the case of $[STO]_9/[NTO]_1$, electrons compensating the charge of the $[NdO]^+$ plane are localized within the TiO_2 planes immediately adjacent to the NdO plane (Figure 6a), while the rest of the STO is unaffected. As t increases, the NTO LHB develops, and the Fermi level moves up until it becomes degenerate with the bottom of the STO conduction band, as is apparent for $[STO]_6/[NTO]_4$ in Figure 6b. To further demonstrate this degeneracy, we show the average electrostatic potential calculated for $[STO]_6/[NTO]_6$ and the band edges of STO and NTO in Figure 6c. The latter were determined relative to their respective average electrostatic potentials in pure STO and NTO coherently strained to the LSAT lattice.[47] Projected densities of states for the $[STO]_6/$

was held constant at 8 u.c. for both the buffer layer and the capping layer unless specified otherwise. Details of the growth, stoichiometry control, and structural characterization of these films are discussed elsewhere.[22] Here, the deposition process is briefly summarized. A 500 nm thick Ta layer was sputter-deposited at room temperature on the back of the substrate prior to the film growth to improve heat transfer between the film and the substrate heater. Titanium tetra-isopropoxide (TTIP) (99.999% from Sigma-Aldrich, USA) was utilized as the metal-organic precursor for Ti source, and solid elemental sources for Nd (99.99% from Ames Lab, USA) and Sr (99.99% from Sigma-Aldrich, USA). No additional oxygen was used since TTIP also supplies oxygen.

Structural characterizations were performed using in situ reflection high-energy electron diffraction (RHEED) (Staib Instruments) and a range of ex situ techniques including high-resolution X-ray diffraction, high-resolution XPS, AFM, STEM, and EELS. Coupled 2θ–ω scans and GIXR using a Philips Panalytical X'Pert thin-film diffractometer with Cu $K\alpha$ radiation were used to determine the out-of-plane lattice parameter, interface roughness, and film thickness (consistent with the thickness determined using STEM and RHEED oscillations), respectively. AFM in contact mode was used to determine the surface morphology. High-resolution core-level and valence band XPS spectra were acquired using monochromatic Al $K\alpha$ X-rays ($h\nu = 1486.6$ eV) and a VG/Scienta R3000 electron energy analyzer. All spectra were measured in the normal-emission geometry and with a total energy resolution of 0.45 eV.

An aberration-corrected monochromatic FEI Titan G2 60-300 STEM equipped with a CEOS DCOR probe corrector was used for STEM analyses. The microscope was operated at 300 keV for HAADF imaging and at 200 keV for EELS measurements with simultaneous acquisition of HAADF images. The semiconvergent angle of the incident beam was 25 mrad at 300 keV and 17 mrad at 200 keV with monochromator ON. HAADF images were obtained with a detector inner angle of 50 mrad at 300 keV and 39 mrad at 200 keV. Monochromatic EELS data were recorded using Gatan Enfinium ER spectrometer with a dispersion of 0.1 eV per channel. Probe current and beam dwell time for EELS acquisition were controlled to avoid detectable specimen damage and to minimize the effect of specimen drift. A dual EELS mode was used to acquire simultaneously both zero-loss and core-loss EELS spectra so that energy drifts during acquisition were compensated and possible chemical shifts can be detected.

DC transport measurements were performed in a physical property measurement system (quantum design) using the van der Pauw geometry. 300 nm of Au on top of 50 nm of Ti were sputtered as ohmic contacts for the NTO/STO/LSAT heterostructures, while 300 nm of Au on 20 nm Ni on top of 40 nm of Al were sputtered as ohmic contacts for STO/NTO/STO/LSAT structures. The contacts were deposited such that they make the direct contact with the 2DEGs at the interfaces. This was achieved by masking the four corners of the sample during MBE growth using metal supporting pins, which are also used to hold the sample. As a result of these pins, no film was deposited at the corner of the sample exposing the film cross section. Metal electrodes were then deposited at the four corners resulting in a direct contact with the 2DEG as illustrated in Figure 2a,d.

For the Hall measurements the magnetic field B was varied between ±9 T. The Hall carrier concentration (n_{2D}) and the mobility (μ) were calculated as $n_{2D} = -1/(e \times R_H)$, and $\mu = 1/(e \times R_s \times n_{2D})$, respectively, where R_H is the measured 2D Hall coefficient and R_s is the measured sheet resistance.

Computational modeling was performed using DFT. The exchange-correlation functional developed by Perdew, Burke, and Ernzerhof (PBE)[50] and revised for solids (PBEsol)[51] was employed and projector-augmented wave potentials,[52] and periodic model as implemented in the Vienna Ab-initio Simulation Package code.[53,54] The Hubbard correction was applied to the Ti 3d states within the DFT+U approach.[55] The lateral cell corresponds to the orthorhombic cell of bulk NTO with in-plane lattice parameters $a = 5.525$ Å and $b = 5.659$ Å. The number of unit cell layers ($n + m$) of [STO]$_n$/[NTO]$_m$ heterostructures was varied such that $10 \leq n + m \leq 14$. The lateral cell of each system was constrained ($a = b = 5.4702$ Å) in order to mimic strain induced by

the LSAT substrate. The geometrical structure of each heterostructure was determined using a two-step procedure. First, the total energy was minimized with respect to the c-axis lattice parameter and the internal coordinates using $U = 2.8$ eV for all Ti atoms. (This value of U was preoptimized so as to reproduce the NTO bulk band gap of 0.8 eV. The lattice parameters of the bulk STO and NTO determined using $U = 2.8$ eV are ≈1% larger than the corresponding experimental values.) Then, the lattice parameters were fixed and the internal coordinates were reoptimized using: (i) $U = 8.0$ eV for the Ti atoms confined by SrO planes (the corresponding STO bulk band gap is ≈3 eV), (ii) $U = 2.8$ eV for the Ti atoms confined by two NdO planes, and (iii) the arithmetic average of these U values for Ti atoms at the interface. This set of parameters was used unless stated otherwise. The $4 \times 4 \times 1$ Monkhorst–Pack grid[56] was used for geometry optimization and $6 \times 6 \times 2$ grid for final electronic structure calculations. All calculations were carried out with the plane-wave cut-off of 500 eV and in the spin-polarized mode. Since the Néel temperature of the bulk NTO is ≈ 95 K and many measurements were performed at room temperature, a broadening of the occupied Ti 3d band due to spin disorder is expected. To account for this effect, electrons occupying this band to be ferromagnetically ordered were considered. The charge density distribution was analyzed using the Bader method.[57,58]

Supporting Information

Supporting Information is available from the Wiley Online Library or from the author.

Acknowledgements

[1] H. Kroemer, *Nobel Lecture*, The Nobel Prize in Physics 2000, Stockholm University, Sweden, December, **2000**.

[2] J. Heber, *Nature* **2009**, *459*, 29.

[3] J. Mannhart, D. G. Schlom, *Science* **2010**, *327*, 1607.

[4] N. Nakagawa, H. Y. Hwang, D. A. Muller, *Nat. Mater.* **2006**, *5*, 204.

[5] H. Y. Hwang, Y. Iwasa, M. Kawasaki, B. Keimer, N. Nagaosa, Y. Tokura, *Nat. Mater.* **2012**, *103*, 11.

[6] A. Gozar, G. Logvenov, L. F. Kourkoutis, A. T. Bollinger, L. A. Giannuzzi, D. A. Muller, I. Bozovic, *Nature* **2008**, *455*, 782.

[7] J. Chakhalian, J. W. Freeland, G. Srajer, J. Strempfer, G. Khaliullin, J. C. Cezar, T. Charllton, R. Dalgliesh, C. Bernhard, G. Cristian, H.-U. Habermeier, B. Keimer, *Nat. Phys.* **2014**, *2*, 244.

[8] A. F. Santander-Syro, F. Fortuna, C. Bareille, T. C. Rödel, G. Landolt, N. C. Plumb, J. H. Dil, M. Radović, *Nat. Mater.* **2014**, *13*, 1085.

[9] P. Zubko, S. Gariglio, M. Gabay, P. Ghosez, J.-M. Triscone, *Annu. Rev. Condens. Matter Phys.* **2011**, *2*, 141.

[10] D. G. Schlom, J. Mannhart, *Nat. Mater.* **2011**, *10*, 168.

[11] E. Dagotto, Y. Tokura, *MRS Bull.* **2008**, *33*, 1037.

[12] S. Stemmer, A. J. Millis, *MRS Bull.* **2013**, *38*, 1032.

[13] E. N. Jin, L. Kornblum, D. P. Kumah, K. Zou, C. C. Broadbridge, J. H. Ngai, C. H. Ahn, F. J. Walker, *APL Mater.* **2014**, *2*, 116109.

[14] M. Dyakonov, M. Shur, *Phys. Rev. Lett.* **1993**, *73*, 2465.

[15] M. S. R. V. Shur, *Int. J. High Speed Electron. Syst.* **2003**, *13*, 575.

[16] B. S. Rodriguez, L. Lei, P. Fay, D. Jena, H. G. Xing, *IEEE Trans. Terahertz Sci. Technol.* **2013**, *3*, 200.

[17] A. Ohtomo, H. Y. Hwang, *Nature* **2004**, *427*, 423.

[18] J. W. Park, D. F. Bogorin, C. Cen, D. A. Felker, Y. Zhang, C. T. Nelson, C. W. Bark, C. M. Folkman, X. Q. Pan, M. S. Rzchowski, J. Levy, C. B. Eom, *Nat. Commun.* **2010**, *1*, 94.

[19] M. L. Reinle-Schmitt, C. Cancellieri, D. Li, D. Fontaine, M. Medarde, E. Pomjakushina, C. W. Schneider, S. Gariglio, P. Ghosez, J. M. Triscone, P. R. Willmott, *Nat. Commun.* **2012**, *3*, 932.

[20] T. A. Cain, P. Moetakef, C. A. Jackson, S. Stemmer, *Appl. Phys. Lett.* **2012**, *101*, 111604.

[21] P. Moetakef, T. A. Cain, D. G. Ouellette, J. Y. Zhang, D. O. Klenov, A. Janotti, C. G. V. d. Walle, S. Rajan, S. J. Allen, S. Stemmer, *Appl. Phys. Lett.* **2011**, *99*, 232116.

[22] P. Xu, D. Phelan, J. S. Jeong, K. A. Mkhoyan, B. Jalan, *Appl. Phys. Lett.* **2014**, *104*, 082109.

[23] M. P. Mikhailova, K. D. Moiseev, Y. P. Yakovlev, *Semicond. Sci. Technol.* **2004**, *19*, 109.

[24] H. Kroemer, *Physica E* **2004**, *20*, 196.

[25] D. Jena, *Proc. IEEE* **2013**, *101*, 1585.

[26] A. Ohtomo, D. A. Muller, J. L. Grazul, H. Y. Hwang, *Nature* **2002**, *419*, 378.

[27] S. Okamoto, A. J. Millis, *Nature* **2004**, *428*, 630.

[28] S. Yunoki, A. Moreo, E. Dagotto, S. Okamoto, S. S. Kancharla, A. Fujimori, *Phys. Rev. B* **2007**, *76*, 064532.

[29] I. Gonzalez, S. Okamoto, S. Yunoki, A. Moreo, E. Dagotto, *J. Phys.: Condens. Matter* **2008**, *20*, 264002.

[30] A. Bhattacharya, S. J. May, *Annu. Rev. Mater. Res.* **2014**, *44*, 65.

[31] H. Chen, A. J. Millis, C. A. Marianetti, *Phys. Rev. Lett.* **2013**, *111*, 116403.

[32] F. Y. Bruno, R. Schmidt, M. Varela, J. G. Barriocanal, A. R. Calzada, F. A. Cuellar, C. Leon, P. Thakur, J. C. Cezar, N. B. Brookes, M. G. Hernandez, E. Dagotto, S. J. Pennycook, J. Santamaria, *Adv. Mater.* **2013**, *25*, 1468.

[33] Y. Xie, Y. Hikita, C. Bell, H. Y. Hwang, *Nat. Commun.* **2011**, *2*, 494.

[34] A. Janotti, L. Bjaalie, L. Gordon, C. G. V. d. Walle, *Phys. Rev. B* **2012**, *86*, 241108.

[35] S. A. Chambers, in *Hard X-Ray Photoelectron Spectroscopy (HAXPES)* (Ed: J. Woicik), Springer, Berlin, Germany **2015**.

[36] S. A. Chambers, Y. Liang, Z. Yu, R. Droopad, J. Ramdani, K. Eisenbeiser, *Appl. Phys. Lett.* **2000**, *77*, 1662.

[37] S. A. Chambers, T. C. Droubay, C. Capan, G. Y. Sun, *Surf. Sci.* **2012**, *606*, 554.

[38] E. A. Kraut, R. W. Grant, J. W. Waldrop, S. P. Kowalczyk, *Phys. Rev. Lett.* **1980**, *44*, 1620.

[39] E. A. Kraut, R. W. Grant, J. W. Waldrop, S. P. Kowalczyk, *Phys. Rev. B* **1983**, *28*, 1965.

[40] A. S. Sefat, J. E. Greedan, G. M. Luke, M. Niewczas, J. D. Garrett, H. Dabkowska, A. Dabkowski, *Phys. Rev. B* **2006**, *74*, 104419.

[41] J. B. Goodenough, *Structure and Bonding*, Springer-Verlag, New York **1998**.

[42] S. J. May, A. B. Shah, S. G. E. t. Velthuis, M. R. Fitzsimmons, J. M. Zuo, X. Zhai, J. N. Eckstein, S. D. Bader, A. Bhattacharya, *Phys. Rev. B* **2008**, *77*, 174409.

[43] A. S. Sefat, G. Amow, M. Y. Wu, G. A. Botton, J. E. Greedan, *J. Solid State Chem.* **2005**, *178*, 1008.

[44] D. G. Ouellette, P. Moetakef, T. A. Cain, J. Y. Zhang, S. Stemmer, D. Emin, S. J. Allen, *Sci. Rep.* **2013**, *3*, 3284.

[45] L. Bjaalie, D. G. Ouellette, P. Moetakef, T. A. Cain, A. Janotti, B. Himmetoglu, S. J. Allen, S. Stemmer, C. G. Van deWalle, *Appl. Phys. Lett.* **2015**, *106*, 232103.

[46] P. Moetakef, T. A. Cain, *Thin Solid Films* **2015**, *583*, 129.

[47] K. T. Delaney, N. A. Spaldin, C. G. Van de Walle, *Phys. Rev. B* **2010**, *81*, 165312.

[48] P. Moetakef, C. A. Jackson, J. Hwang, L. Balents, S. J. Allen, S. Stemmer, *Phys. Rev. B* **2012**, *86*, 201102.

[49] L. Bjaalie, A. Janotti, B. Himmetoglu, C. G. Van de Walle, *Phys. Rev. B* **2014**, *90*, 195117.

[50] J. P. Perdew, K. Burke, M. Ernzerhof, *Phys. Rev. Lett.* **1996**, *77*, 3865.

[51] J. P. Perdew, A. Ruzsinszky, G. I. Csonka, O. A. Vydrov, G. E. Scuseria, L. A. Constantin, X. Zhou, K. Burke, *Phys. Rev. Lett.* **2008**, *100*, 136406.

[52] P. E. Blöchl, *Phys. Rev. B* **1994**, *50*, 17953.

[53] G. Kresse, J. Furthmüller, *Phys. Rev. B* **1996**, *54*, 11169.

[54] G. Kresse, D. Joubert, *Phys. Rev. B* **1999**, *59*, 1758.

[55] S. L. Dudarev, G. A. Botton, S. Y. Savrasov, C. J. Humphreys, A. P. Sutton, *Phys. Rev. B* **1998**, *57*, 1505.

[56] H. J. Monkhorst, J. D. Pack, *Phys. Rev. B* **1976**, *13*, 5188.

[57] R. F. W. Bader, *Atoms in Molecule—A Quantum Theory*, Oxford University Press, Oxford **1990**.

[58] W. Tang, E. Sanville, G. Henkelman, *J. Phys.: Condens. Matter* **2009**, *21*, 084204.